Experimental Verification of Singularity-Robust Torque Control for a 1.2-Nm–5-Hz SGCMG

Sangdeok Lee, *Graduate Student Member, IEEE*, and Seul Jung, *Member, IEEE*

***Abstract*—A single gimbal control moment gyro (SGCMG) has been designed and developed as a torque amplifier to generate 1.2-Nm–5-Hz gyroscopic torque for the angle deviation of 45°. Since the SGCMG is aimed to generate the torque accurately in the designated direction, the return of the gimbal from the disturbance should be guaranteed within a desired frequency. However, unexpected axial drift exists and leads to a null motion under the torque control scheme. Therefore, this paper identifies the cause of axial drift and proposes a new torque control technique with two phases of compensation. Compensator I is designed to eliminate the nonlinear axial drift modeled as a sigmoidal function through an empirical identification process. Compensator II reduces other uncertainties by integrating high-pass filtering, recursive least square, all pass filtering, and moving average filtering (MAF) process. Finally, the proposed control scheme has been verified through experimental studies.**

***Index Terms*—Axial drift, compensation, control moment gyroscope (CMG), robust torque control, singularity.**

I. Introduction

CMGS (control moment gyroscopes) have been used effectively to amplify torques where direct torques cannot be applied due to the design complexity or specifications of a target system structure [1]. CMGs are also utilized in various systems to control attitude such as those used in space systems, especially for the maneuver of satellite systems [2], [3], and underwater robotic systems [4].

CMGs may also be used in more challenging tasks such as a core actuator to balance the angle of single-wheel robotic systems that maintain balance while moving forward and backward [5]–[7].

CMGs have to generate a torque in the yaw direction (heading) for single wheel robots to balance in the roll (lateral) direction by the relation with the friction on the ground.

It was discovered during the development of single wheel robots that the design and control of a gimbal to manipulate torque and return time were key roles for a successful CMG. Since the gyroscopic torque is induced by combining both the angular momentum of the flywheel and the angular rate of the gimbal, there is always a trade-off in design between torque and return time (or frequency). It is quite difficult for CMGs to satisfy both accurate torque and desired frequency.

By the nature of rotational dynamics, the output torque direction changes with time, and its magnitude is reduced with respect to the axial position of the gimbal system. Ultimately, CMGs may end up with a singular position resulting in no induced torque. Therefore, avoiding/escaping singularities (null motion) has been a main crucial problem in the control applications of CMGs.

The singularity of a single CMG occurs in the control of single-wheel robots to regulate the balancing [5], [6]. The singularity happens when the gimbal leans against one direction beyond a certain angle resulting in null motions. The singularity of CMG has been addressed when multiple CMGs are used to form a redundant configuration [8], [9]. In a cluster structure of several CMGs, it is highly desirable that all CMG actuators work together to avoid singularities.

A redundant actuator approach has been widely used to avoid singularity by adding extra actuators to remedy the singular motion. Since the configuration of multiple SGCMGs or Dual gimbal CMGs have various topologies, their structures become too complex, and control becomes quite difficult [10], [11]. Varying speed control of a SGCMG was done by adding a magnitude change function to improve the maneuverability under the condition of rapid flywheel speed change [12]. Above all, the redundant approach is so complex, and control is too difficult.

Meanwhile, a current control technique is fast and simple, and the exact torque maneuverability can be achieved without adding extra actuators. This technique requires a fast return time. The worst case is the null motion of CMG when the axis of the gimbal rotates 90° and loses the ability to control the torque. This gimbal angle drift makes the SGCMG fail to generate the necessary torque and leads to the system instability.

Although the position control of the gimbal axis can solve this problem with ease, generating an effective torque quickly is difficult and the resulting performance degrades dramatically. The position control cannot provide the CMG with enough agility, but the torque control technique can provide desired agility to CMG.

However, torque control suffers from the axial drift of the gimbal system due to uncertain variables, such as vibration,

Manuscript received March 8, 2017; revised July 18, 2017; accepted September 25, 2017. Date of publication October 12, 2017; date of current version February 13, 2018. This work was supported by the National Research Foundation of South Korea under Grant 2016 R1A2B2012031. *(Corresponding author: Seul Jung.)*

The authors are with the Department of Mechatronics Engineering, Chungnam National University, Daejeon 34134, South Korea (e-mail: sdcon.lee@cnu.ac.kr; jungs@cnu.ac.kr).

Color versions of one or more of the figures in this paper are available online at http://ieeexplore.ieee.org.

Digital Object Identifier 10.1109/TIE.2017.2762619

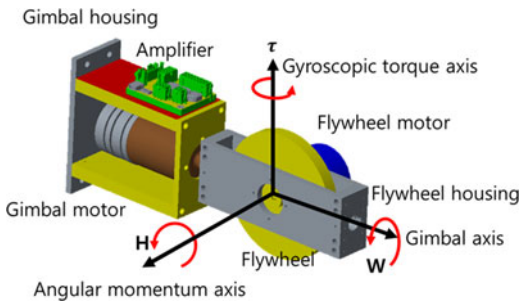

Fig. 1. Design of a SGCMG.

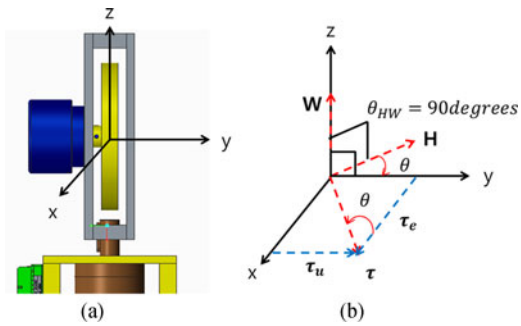

Fig. 2. Coordinates of the SGCMG system.

flywheel (rotor) imbalance [13], joint friction [14]–[16], and harmonics from the electronics [17]. From a structural point of view, the axial misalignment must be corrected to achieve the robust control performance [18]. Chances of falling into null motion are increased by the axial drift condition under current torque control techniques.

Therefore, in this paper, a novel robust torque control method is proposed to avoid the singularity. Two compensation phases are designed. The first compensation is for the axial drift by modeling it as a sigmoidal function through an extensive empirical process. Compensator II is designed by cascading several processes including high pass filtering (HPF) to eliminate low frequency components of uncertainties, model identification by RLS, and stabilization by APF to compensate for other uncertainties [19]–[22]. The identified inverse model is used to cancel uncertainties in the disturbance observer (DOB) framework. Experimental studies are conducted to confirm the control performance and evaluate the effect on the accuracy of torque and the agility of return time.

II. SGCMG Design

A SGCMG is designed to generate the regulated torque performance as illustrated in Fig. 1. The actuator consists of two blushless motor systems. The flywheel motor is mounted to generate angular momentum at a constant speed and the gimbal system is orthogonally mounted to the direction of the angular momentum. The finalized torque direction is also orthogonal to both the angular momentum and the gimbal rotating direction.

The gyroscopic torque is induced by combining two physical properties, the angular momentum of a flywheel and the tilting rate of the gimbal. Regulating the rotational speeds of both a flywheel and a gimbal controls the magnitude and direction of the induced torque. The principle of the induced torque for SGCMG can be described as a cross product of two physical quantities

$$\tau = \boldsymbol{H} \times \boldsymbol{W} \tag{1}$$

where $\tau(\mathrm{Nm})$ is the gyroscopically induced torque vector, $\boldsymbol{H}(\mathrm{N \cdot m \cdot s/rad})$ is the angular momentum vector of a flywheel, and $\boldsymbol{W}(\mathrm{rad/s})$ is the angular rate vector of a gimbal system.

The coordinates of the gyroscopic torque can be configured as shown in Fig. 2.

From Figs. 1 and 2(b), the induced torque becomes

$$\tau = HW \sin(\theta_{HW}) = HW \tag{2}$$

where θ_{HW} is always 90° in the SGCMG.

From the configuration in Fig. 2(b), the induced gyroscopic torque can be decomposed into two vectors according to the angle position of the gimbal axis:

$$\tau = \tau_e + \tau_u \tag{3}$$

where τ_e is the effective torque and τ_u is the unexpected toque. The effective torque is defined as follows:

$$\tau_e = HW \cdot \cos(\theta) \tag{4}$$

where H is a momentum of a flywheel, W is the magnitude of the gimbal rate, and θ is the angle position of the gimbal axis. Definitely, minimizing the unexpected torque is desired by forcing the gimbal angle, θ to zero. The induced torque can be maximized by guaranteeing the fast return of the gimbal axis. This is our goal in this paper.

III. SGCMG Characterization

A. Electromechanical Properties of SGCMG

A SGCMG has been developed as an indirect actuator to manipulate the orientation of a target system. To perform a desired actuation task, a SGCMG or other CMGs must be designed to satisfy the specifications of torque specifications and return frequency considering the dynamic control range of the target system. Here our SGCMG is designed specifically to generate 1.2 Nm torque with 5 Hz return frequency for the angle deviation of 0.25π(radian) as described in Fig. 3. The corresponding electro-mechanical properties of the SGCMG are listed in Table I.

The angular momentum has a linear relationship with the inertia and the angular velocity of the flywheel as

$$H = I_f \dot{\theta}_f \tag{5}$$

where H is the magnitude of the angular momentum $\boldsymbol{H}$, I_f is the moment of inertia of the flywheel, and $\dot{\theta}_f$ is the angular rate of the flywheel. The constant angular momentum, H of our SGCMG is set to be $0.201(Nm \cdot s/rad)$.

Since $\boldsymbol{H}(Nm \cdot s/rad)$ is set to be constant by the flywheel system, the torque of a gimbal system is controlled by the angular velocity $\boldsymbol{W}(rad/s)$ in (1). Our main concern is how to

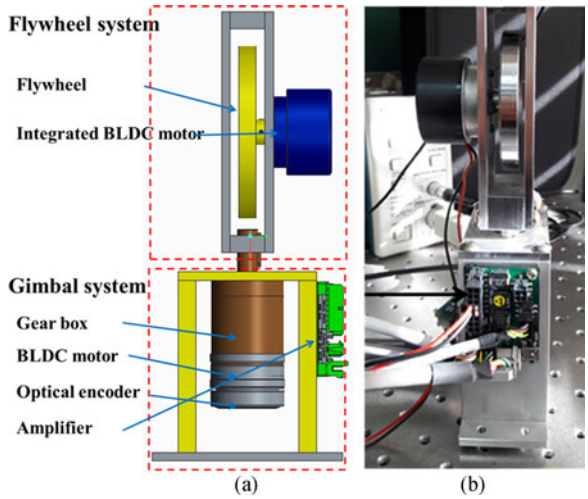

Fig. 3. Conceptual drawing and an actual gyroscopic actuator. (a) Design. (b) SGCMG.

TABLE I
ELECTRO-MECHANICAL PROPERTIES OF A SGCMG

Category	Items	Values	Units
Form factor	Weight	1.58	Kg
	Size	240 × 110 × 80	mm
Flywheel motor	Model	EC-45	–
	Capacity	30	W
	Supply voltage	24	V
	Nominal current	2.02	A
	Maximum current	4.41	A
	Nominal speed	6000	rpm
	Nominal torque	58.2	Nm
Gimbal motor	Model	EC-45	–
	Capacity	30	W
	Supply voltage	24	V
	Nominal speed(No load)	4630	rpm
	Nominal current	1.01	A
	Maximum current	4.93	A
Gear box	Ratio	21:1	–
System	Weight	1.58	Kg
	Size	240 × 110 × 80	mm
	Angular momentum of flywheel	0.201	Nm-s/rad
	Maximum gimbal rate	9.4	rad/s

control the current or the torque to the gimbal system in order to satisfy the desired specifications.

B. Effective Torque Estimation

As a torque amplifier, the output torque must have a linear amplification property with respect to the input torque, namely the input current. The input current is considered to be a sinusoidal signal as

$$i_c = I_c \sin(2\pi \mathrm{ft}) \tag{6}$$

where I_c is the maximum current and f is the control frequency.

According to (3) and (4), the effective torque can be empirically estimated by investigating the output torque with respect to different input current values, I_c from 0.1 to 0.9 A. The overall input currents are measured as shown in Fig. 4(a). Specifically, the input current is limited to 0.9 A due to the amplifier limitation. The corresponding output torque to the input current is shown in Fig. 4(b).

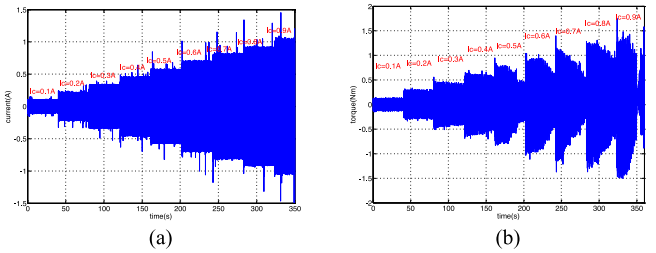

Fig. 4. Effective torque characteristic for input current. (a) The input current. (b) The output torque.

TABLE II
MAXIMUM OUTPUT TORQUES TO INPUT CURRENTS

I_C (A)	0.1	0.2	0.3	0.4	0.5	0.6	**0.7**	**0.8**	**0.9**
τ(Nm)	0.14	0.33	0.55	0.7	0.96	1.13	**1.46**	**1.39**	**1.9**

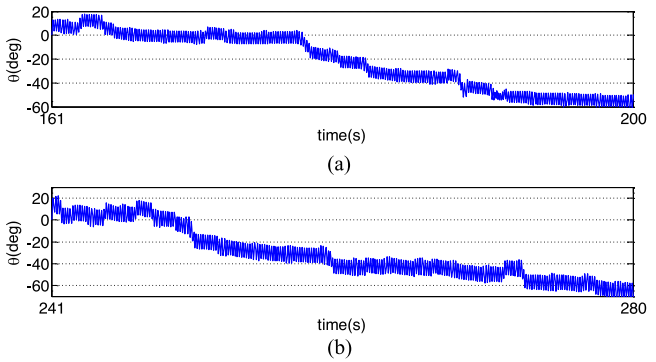

Fig. 5. Gimbal angle with respect to input currents. (a) Case 1 : 0.5 A. (b) Case 2 : 0.7 A.

The output torque tends to decrease due to the occurrence of the gimbal angle deviation. The unexpected torque, τ_u leads to the reduction of the resulting torque magnitude, τ_e in (4).

The maximum value of an output torque with respect to an input current is listed in Table II. Considering the design factor of a 1.2 Nm induced torque, the supplied input current should be higher than 0.7 A.

C. Gimbal Angle Drift Investigation

When the input currents are given, the gimbal angles are observed as shown in Fig. 5. Since the angle deviation appears severely after the input current of 0.5 A, the current input steps from 0.5 to 0.9 A were investigated for the drift of the gimbal angle, θ. Two cases of different inputs are shown in Fig. 5 and both cases show a similar pattern of angle drift over time.

This drift problem can be clearly characterized in the frequency domain. Fig. 6 shows the corresponding frequency responses. There are dominant frequency characteristics at around 6 Hz, which means that a regulated torque is generated to satisfy the return frequency of 5 Hz.

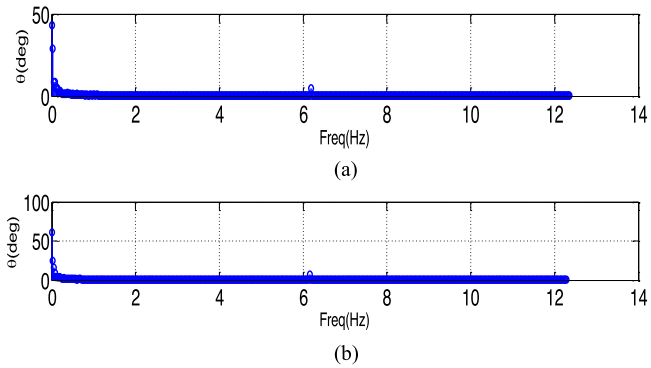

Fig. 6. Gimbal angle in the frequency domain. (a) Case 1 : 0.5 A. (b) Case 2 : 0.7 A.

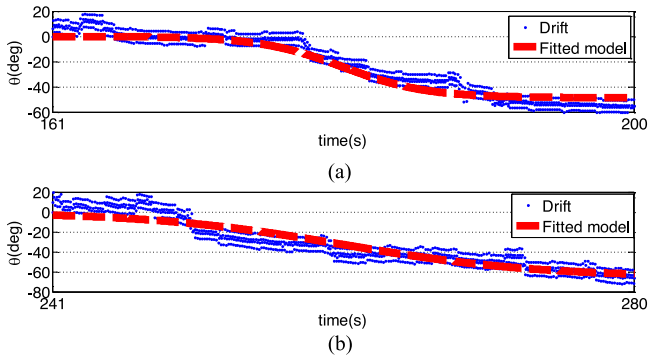

Fig. 7. Sigmoid function models for Fig. 5. (a) Fitted model for Fig. 5 (a). (b) Fitted model for Fig. 5 (b).

Note that the gimbal angle has components at around 0 Hz as well. These components are considered as an undesired axial drift. Therefore, the axial drift can be characterized as a low frequency component. The angle drift must be minimized to guarantee the regulated torque output under the torque control of SGCMG.

D. Modeling of Axial Drift

Investigating Fig. 5 carefully, the axial drift can be modeled as a sigmoidal function defined as

$$\hat{n}(\theta, W) = \frac{\alpha}{1+e^{\beta \nabla t}} + \delta, \left\{ \begin{array}{l} \alpha(t) = C, -\infty < \beta(t) < +\infty \\ \nabla t = T, \delta < n < (\alpha + \delta) \end{array} \right\} \tag{7}$$

$$\alpha = \frac{\theta}{\hat{\theta}_{\mathrm{SAT}}}, \beta = W_{\mathrm{average}}, \nabla t = T_{\mathrm{ELAPSED}}(t) \tag{8}$$

where $\hat{\theta}_{\mathrm{SAT}}$ is the expected saturation angle at time t, W_{average} is the average gimbal rate at time t, T_{ELAPSED} is the elapsed time during the certain control period, and δ is an offset. By adjusting four parameters, such as α,β, δ, and ∇t during the control period, the axial drift of $\hat{n}(\theta, W)$ can be estimated.

Approximated models of Fig. 5 are shown in Fig. 7. Fig. 5(a) can be modeled as $\hat{n}_1(\theta, W) = \frac{-48.63}{1+e^{-0.349(t-20)}}$ and Fig. 5(b) as $\hat{n}_2(\theta, W) = \frac{-65.32}{1+e^{-0.149(t-20)}}$. Since these models contain some offsets all the time, the offset compensation technique is required along with a sigmoidal model-based compensator.

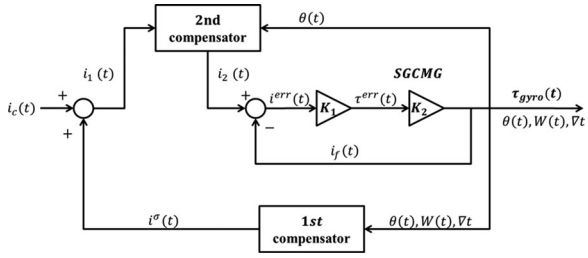

Fig. 8. Proposed torque control scheme.

IV. SGCMG Torque Control Scheme

A. Compensation I: Axial Drift Compensation

SGCMG is modeled as a second-order system and the general description of second-order mechanical systems is as follows [23]:

$$M_a(\theta)\dot{W} + B_a(\theta, W)W + n_a(\theta, W) = \tau_{\mathrm{gyro}} \tag{9}$$

where $M_a(\theta)$ is the nominal model of the inertia term, $B_a(\theta, W)$ is the nominal model term of the Coriolis and centrifugal force, $n_a(\theta, W)$ is the uncertainty, and τ_{gyro} is the gyro torque.

Since we have the axial drift model, the drift can be compensated as described in Fig. 8. In compensation I, the nonlinear term is identified and compensated.

In Fig. 8, i_c is the input current, i_1 is the first compensated current, i_2 is the second compensated current, i^{σ} is the first compensating current, i^{err} is the error current, K_1 is the current amplification gain in the amplifier, K_2 is the torque amplification factor of SGCMG, τ^{err} is the torque error, i_f is the current feedback, θ is the axial angle position, W is the angular rate, ∇ is the elapsed time, and τ_{gyro} is the magnitude of the gyroscopic torque.

The first compensation current is given as

$$i_1 = i_c + i^{\sigma} = i_c + \hat{n}(\theta, W). \tag{10}$$

The closed error model becomes

$$M_a\dot{W} + B_aW + n_a(\theta, W) = i_c + \hat{n}_a(\theta, W). \tag{11}$$

After the first compensation, the modeling error occurs as

$$M_a\dot{W} + B_aW + \delta_a = i_c. \tag{12}$$

where δ_a is the axial drift modeling error.

B. Compensation II : Axial Drift Compensation

The control law for the second compensation becomes

$$\tau = K_1K_2(i_2 - i_f). \tag{13}$$

At the steady state, $i_f \approx 0$ can be assumed and (12) becomes

$$M_a\dot{W} + B_aW + \delta_a = Ki_2 \tag{14}$$

where $K = K_1K_2$.

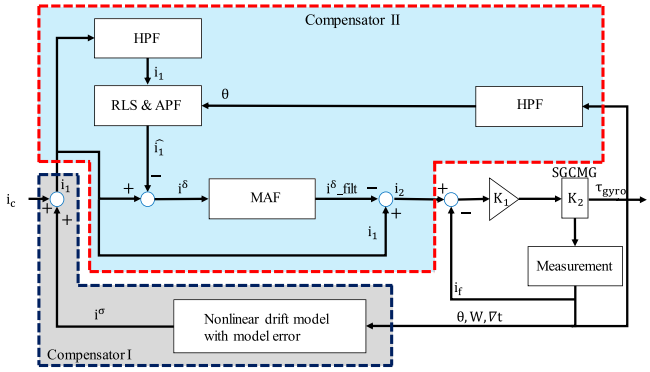

Fig. 9. Two phases compensation control scheme.

The goal of the second compensator is to design the control current i_2 in (14). Since the nonlinear drift has been compensated in the previous section, we have an approximated linear model. Based on the DOB configuration, other disturbances are compensated by the second compensator designed through several processes, shown in Fig. 9.

Process 1 is the high pass filtering for eliminating low frequency uncertainties, process 2 is the RLS process for model identification, process 3 is APF for stabilization of identified models, and process 4 is the moving average filtering (MAF).

1) Process 1: High Pass Filtering: After the first compensation by the axial drift model, (14) can be rewritten as follows:

$$M\dot{W} + BW + \delta = i_2 \tag{15}$$

where $M = \frac{M_a}{K}, B = \frac{B_a}{K}, n = \frac{\hat{n}_a}{K}, \delta = \frac{\delta_a}{K}$.

Although the first compensator minimizes the axial drift phenomenon, there is still a modeling error δ. As analyzed, most of frequency responses are concentrated at the low frequencies less than 0.5 Hz. The drift phenomenon in the low frequency needs to be filtered out.

The high pass filter technique can eliminate the axial drift model error. When HPF is applied to both sides of (15), (15) becomes the discrete domain as

$$HPF\left\{M\dot{W}(n) + BW(n) + \delta(n)\right\} \approx M\dot{W}(n) + BW(n). \tag{16}$$

In real implementation, the HPF was designed with a 5-order Butterworth IIR-filter. The cutoff frequency is 2.5 Hz and the sampling frequency is 12 Hz. The filter has 5 poles inside the unit circle, which shows the stable condition (7), shown at the bottom of this page.

2) Process 2: Recursive Least Square: After passing a high pass filter, (15) can be reduced as follows:

$$M\dot{W} + BW = i_2. \tag{18}$$

Equation (18) becomes

$$P(s) = \frac{\Theta(s)}{I_2(s)} = \frac{1}{Ms^2 + Bs} \tag{19}$$

where $P(s)$ is the nominal model of the given system. In the discrete frequency-domain, (19) can be rewritten as follows:

$$P(z) = \frac{\Theta(z)}{I_2(z)} = \frac{a_1 + a_2 z^{-1} + a_3 z^{-2}}{1 + a_4 z^{-1} + a_5 z^{-2}}, \tag{20}$$

where $P(z)$ is the nominal model of the given system in the discrete frequency-domain.

The inverse the model becomes

$$P^{-1}(z) = \frac{I_2(z)}{\Theta(z)} = \frac{1 + a_4 z^{-1} + a_5 z^{-2}}{a_1 + a_2 z^{-1} + a_3 z^{-2}}. \tag{21}$$

By implementing the model as an adaptive filter, the filter's coefficients are updated through the RLS algorithm. When the unknown system is parameterized as input data and output data as a second order proper function, its parameters can be estimated as follows:

$$y[n] = x^T \varphi[n] \tag{22}$$

$$x[n] = \left(\theta[n-1]\ \theta[n-2]\ i_2[n]\ i_2[n-1]\ i_2[n-2]\right)^T \tag{23}$$

$$\varphi[n] = \left(a_4[n] \quad a_5[n] \quad a_1[n] \quad a_2[n] \quad a_3[n]\right)^T \tag{24}$$

where $y[n]$ is the output data, $x^T[n]$ represents for the input data vector, and $\varphi[n]$ represents for the parameter vector.

Considering the forgetting factor, RLS updates can be done as follows:

$$G[n] = \frac{\frac{1}{\lambda}C[n-1]x[n]}{1 + \frac{1}{\lambda}x^T[n]C[n-1]x[n]} \tag{25}$$

$$C[n] = \frac{1}{\lambda}\left(C[n-1] - G[n]x^T[n]C[n-1]\right) \tag{26}$$

$$\hat{\varphi}[n] = \hat{\varphi}[n-1] + G[n]\left(y[n] - x^T[n]\hat{\varphi}[n-1]\right) \tag{27}$$

where λ is the forgetting factor and its inverse is considered as a memory effect. Here the fixed value of λ is 0.999. For the identified models, stability must be confirmed.

3) Process 3: All Pass Filtering: Since RLS cannot confirm stability of the identified model, estimated parameters should be transformed with a minimum phase model for stability. An all pass filter technique is used and listed in Table III.

4) Process 4: MAF: For more general implementation of $i_2(n)$ in the real system, the sensitivity of the compensator must be considered. To smoothen the signals in Fig. 9, the MAF is used for the filtered command as follows:

$$i_2 = i_1 - i^{\delta}\_filt, t_{\text{delay}} = f(N) \tag{28}$$

where t_{delay} is the delay of the averaging data N.

V. Experimental Verification

A. Experimental Setup

For the vibration-proof, the SGCMG and the sensor system are all mounted on the antivibration desk, as shown in Fig. 10.

$$HPF(z) = \frac{0.0969 - 0.4845z^{-1} + 0.969z^{-2} - 0.969z^{-3} + 0.4845z^{-4} - 0.0969}{1 - 0.8209z^{-1} + 0.8695z^{-2} - 0.3084z^{-3} + 0.09338z^{-4} - 0.008726} \tag{17}$$

TABLE III
APF ALGORITHM FOR THE SECOND ORDER MODEL

a_i : **The estimated parameters**
b_i : **The transformed parameters**
Step 1: Construct the numerator polynomial
$n(z) = a_1(1 + \frac{a_2}{a_1}z^{-1} + \frac{a_3}{a_1}z^{-2})$
Step 2: Find out the two roots for the numerator polynomial
$r_1 = \frac{-\frac{a_2}{a_1} + \sqrt{(\frac{a_2}{a_1})^2 - 4\frac{a_3}{a_1}}}{2}$, $r_2 = \frac{-\frac{a_2}{a_1} - \sqrt{(\frac{a_2}{a_1})^2 - 4\frac{a_3}{a_1}}}{2}$
Step 3: Check for the stabilities of the roots
IF $|r_i| < 1$ **THEN**
$s_i = r_i$ **and** $g_i = 1$
ELSE
$s_i = \frac{1}{r_i}$ **and** $g_i = |s_i|$
END
Step 4: Construct the denominator polynomial
$d(z) = (1 + a_4(n)z^{-1} + a_5(n)z^{-2})$
Step 5: Find out the two roots for the denominator polynomial
$r_3 = \frac{-a_4 + \sqrt{(a_4)^2 - 4a_5}}{2}$, $r_4 = \frac{-a_4 - \sqrt{(a_4)^2 - 4a_5}}{2}$
Step 6: Check for the stabilities of the roots
IF $|r_i| < 1$ **THEN**
$s_j = r_j$ **and** $g_j = 1$
ELSE
$s_j = \frac{1}{r_j}$ **and** $g_j = |s_j|$
END
Step 7: Construct the coefficients b_i
$b_1 = a_1, b_2 = -a_1(s_1 + s_2), b_3 = a_1(s_1 \cdot s_2)$
$b_4 = -(s_4 + s_5), b_5 = (s_4 \cdot s_5)$
Step 8: Update the minimum phase model
$(b_1 + b_2 z^{-1} + b_3 z^{-2})/(1 + b_4 z^{-1} + b_5 z^{-2}) \cdot (g_4 \cdot g_5)/(g_1 \cdot g_2)$

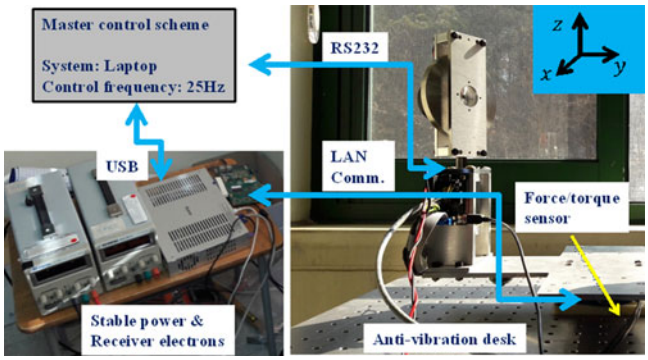

Fig. 10. Experimental setup.

A SGCMG is mounted on the force/torque sensor system. A PC is used as a master controller and the control law is utilized in Visual C++ Software. The control frequency is 25 Hz and the angular rate of the flywheel is set to 6,000 RPM.

Three control schemes are conducted and their results are compared. Scheme 1 is a pure current control without adopting any compensators. Scheme 2 has the first compensator which has no model error compensation. Scheme 3 has both the first compensator and the second compensator.

B. Experiment I: Drift Compensation

1) Control period check: Control period is basically checked before investigating the control performances of three different control schemes.

Table IV and Fig. 11 confirm that the test had been conducted under the reasonable environment.

TABLE IV
CONTROL PERIOD

	Scheme 1	Scheme 2	Scheme 3
Mean(s)	0.0406	0.0404	0.0406
STD.	0.0035	0.0033	0.0031

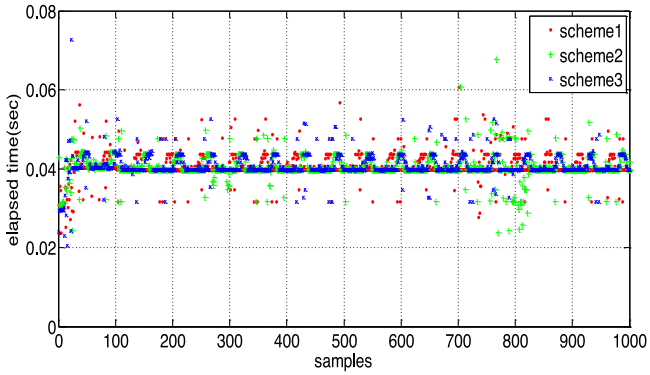

Fig. 11. Control period comparison.

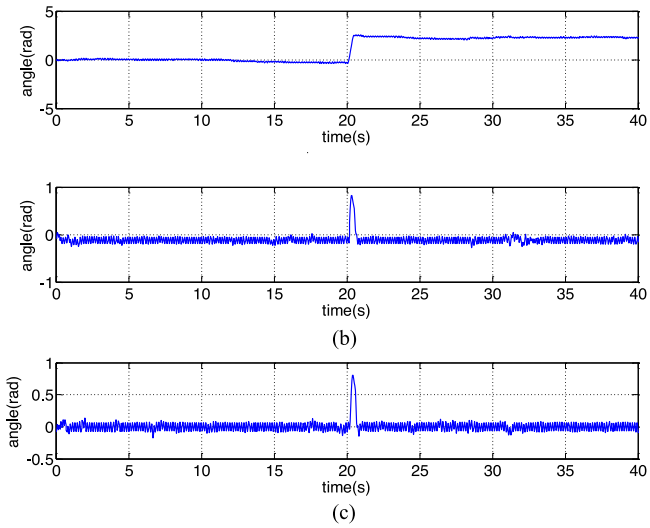

Fig. 12. Angle robustness for external disturbance. (a) Scheme 1. (b) Scheme 2. (c) Scheme 3.

2) Axial angle robustness: In the robustness test, intended disturbance was designed and programmed at 20 seconds after starting the control program. Fig 12 shows the gimbal angles after the disturbance. For Scheme 1 of Fig. 12(a), the angle does not return to the zero position after the external shift. However, both Schemes 2 and 3 show the returning performances in Fig. 12(b) and (c), respectively.

The detailed performance is summarized as in Table V. We see clearly that the angle error of Scheme 3 is the smallest.

3) Gyroscopic Torque Comparison: Since the difference is not clear, the magnitudes in the frequency-domain are compared as shown in Fig. 13. Although Scheme 1 in Fig. 13(a) also shows a better performance than Scheme 2 in Fig. 13(b), the magnitude of Fig. 13(a) is smaller than that of Scheme 3 in Fig. 13(c). Fig. 13(c) shows the exact single tone performance without any jitters. However, Fig. 13(b) shows jitters around

TABLE V
ANGLE ERRORS

	Scheme 1	Scheme 2	Scheme 3
Mean	62.6913	–6.4020	0.0940
Std.	68.0831	5.2812	4.7264

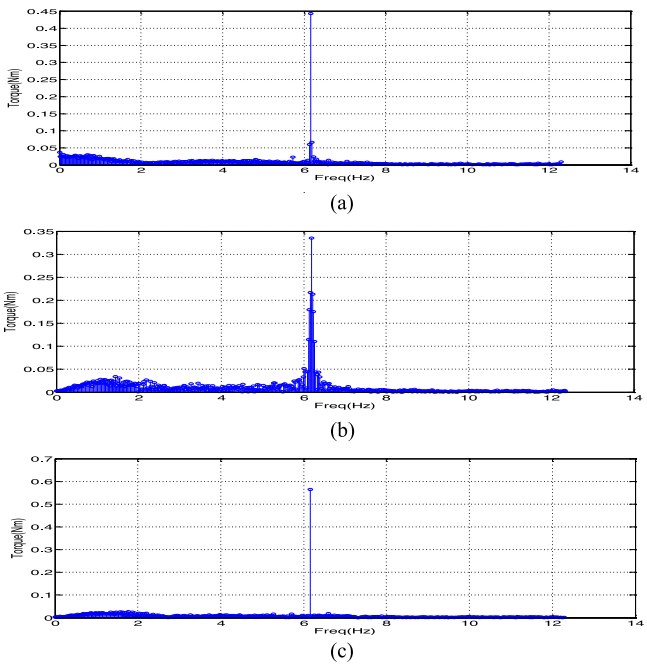

Fig. 13. Gyroscopic torque in the frequency domain. (a) Scheme 1. (b) Scheme 2. (c) Scheme 3.

TABLE VI
GYRO TORQUE MAGNITUDE

	Scheme 1	Scheme 2	Scheme 3
Torque (Nm)	0.45	0.34	0.56

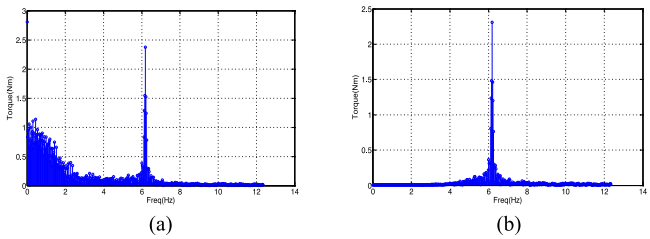

Fig. 14. HPF performance. (a) Before. (b) After.

the frequency of 6 Hz. Therefore, Scheme 3 has the better performance than Scheme 2. Overall, Scheme 3 shows the best performance among all schemes as listed in Table VI.

4) HPF Performance Check: The proposed HPF can successfully remove the offset where the first offset is driven from model uncertainties at 0 Hz and the second offset from disturbances under the 4 Hz. The low frequency components were removed as shown in Fig. 14(b).

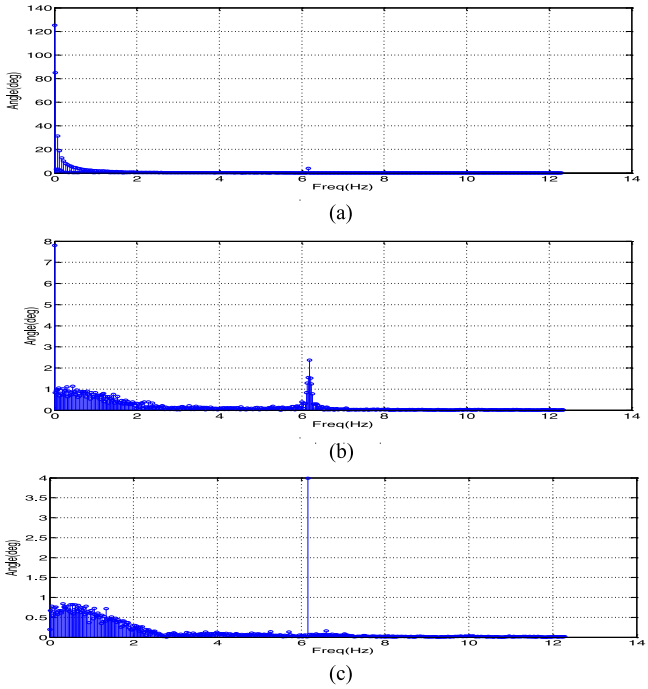

Fig. 15. Offset compensation performance. (a) Scheme 1. (b) Scheme 2. (c) Scheme 3.

TABLE VII
PERFORMANCES OF MODEL ERROR COMPENSATION

	Scheme 1	Scheme 2	Scheme 3
Offset (degree)	125.25	7.80	0.78

5) Offset Compensation Check: The performance of the compensation for the model error has been investigated in the frequency-domain as shown in Fig. 15. Offset values around 0 Hz are minimized for Scheme 3.

The performances are summarized as Table VII.

C. Experiment II: Return Performance

The performance of returning to the desired angle position is tested when the initial angle is arbitrary and unknown disturbances are applied to the system intentionally.

Disturbances by twisting the angle with two fingers are applied such that the gimbal angle is forced to deviate from the desired angle position under torque control at 6.3 s and 11.3 s. Fig. 16 shows the experimental results before and after the first disturbance. We see that the angle returns to its original position.

The corresponding angle plot due to the disturbances is clearly shown in Fig. 17(a). Another twist at 11.3 s is given to the gimbal system in the opposite direction. Similarly, the gimbal returns to the desired position successfully within 0.2 s as shown in Fig. 17(c).

Compensating current is plotted in Fig. 17(b). Since the unexpected current has been compensated by the proposed torque control scheme, the resulting effective torque current is increased.

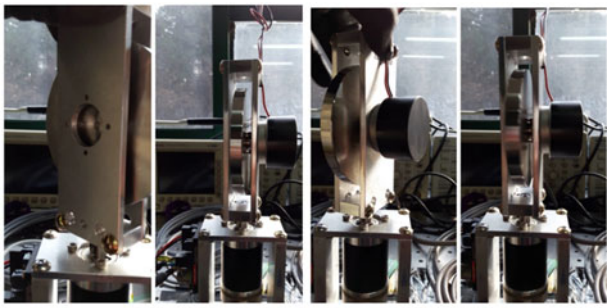

Fig. 16. Return performance under disturbance. (a) First disturbance. (b) Second disturbance.

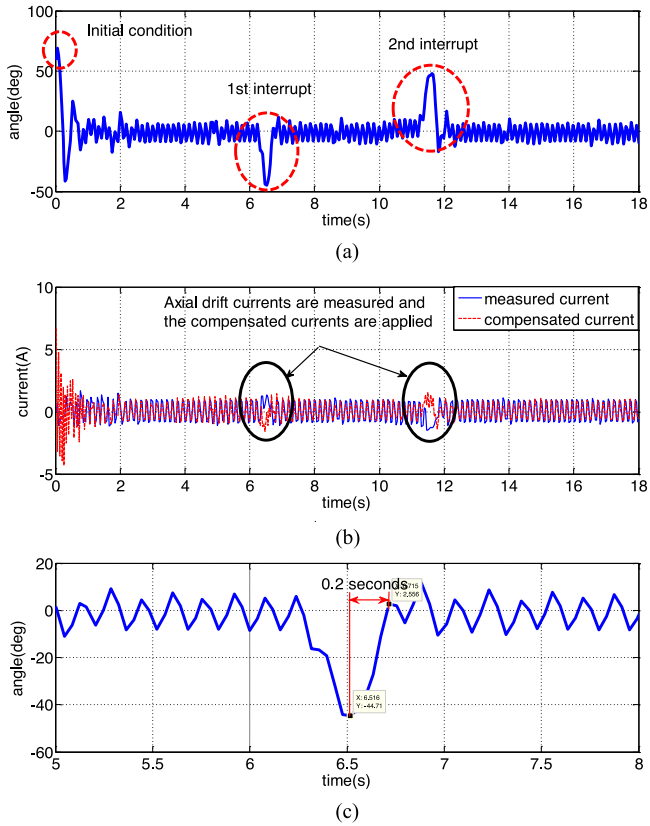

Fig. 17. Compensation performance under disturbance by scheme 3. (a) Angle. (b) Currents. (c) Return time.

This confirms that the proposed torque control scheme actually regulates the deviation of the gimbal angle to the initial position within a specified time of 0.2 s.

D. Experiment III: Torque Regulation

We found from experiments that there are always chaotic torques in the conventional control approach. The unregulated torque without compensation (Scheme 1) is shown in Fig. 18(a), while the well regulated torque is by Scheme 3 in Fig. 18(b).

The proposed control scheme can compensate for uncertainties so that regulated torques in the desired direction can be obtained.

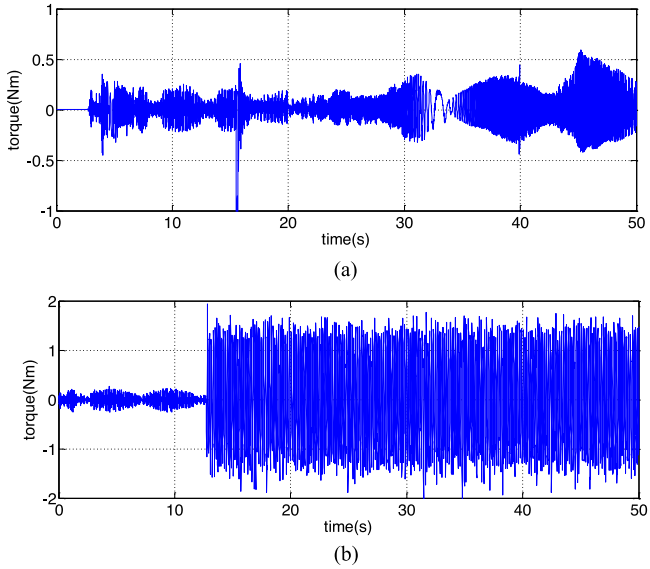

Fig. 18. Comparison of torque characteristics. (a) Scheme1: Conventional control approach. (b) Scheme 3: Proposed control approach: x-direction.

VI. Conclusion

SGCMG was designed, implemented, and controlled to satisfy the specifications of 1.2 Nm-5 Hz. To achieve the singularity-robust torque control performance for SGCMG, a two phases compensation control technique was proposed. The first compensation is for the axial drift of the gimbal system modeled as a sigmoidal function. The second compensation is for other uncertainties through several processes including HPF, RLS, and APF. Extensive experimental studies have been conducted and verified the singularity-robust performance of the gimbal system. This allows us to develop a combined model of multiSGCMGs further for other applications requiring indirect actuation.

References

[1] V. J. Lappas, W. H. Steyn, and C. I. Underwood, "Control moment gyro gimbal angle compensation using magnetic control during external disturbances," *Electron. Lett.*, vol. 37, no. 9, pp. 603–604, 2001.

[2] R. H. Bishop, S. J. Paynter, and J. W. Sunkel, "Adaptive control of space station with control moment gyros," *IEEE Control Syst.*, vol. 12, no. 5, pp. 23–28, Oct. 1992. 1992.

[3] H. Gui, G. Yukovich, and S. Xu, "Attitude tracking of a rigid spacecraft using two internal torques," *IEEE Trans. Aerosp. Electron. Syst.*, vol. 51, no. 4, pp. 2900–2914, Oct. 2015.

[4] B. Thornton, T. Ura, Y. Nose, and S. Turnock, "Zero-G class underwater robots: Unrestricted attitude control using control moment gyros," *IEEE J. Ocean Eng.*, vol. 32, no. 3, pp. 565–583, Jul. 2007.

[5] Y. Xu and S. K. Au, "Stabilization and path following of a single wheel robot," *IEEE/ASME Trans. Mechatronics*, vol. 9, no. 2, pp. 407–419, Jun. 2004.

[6] J. H. Park and S. Jung, "Development and control of a single-wheel robot: Practical mechatronics approach," *Mechatronics*, vol. 23, pp. 594–606, 2013.

[7] Y. Zhu, Y. Gao, C. Xu, J. Zhao, H. Jin, and J. M. Lee, "Adaptive control of gyroscopically stabilized pendulum and its application to a single-wheel pendulum robot," *IEEE/ASME Trans. Mechatron.*, vol. 20, no. 5, pp. 2095–2106, Oct. 2015.

[8] B. Wie, "Singularity analysis and visualization for single-gimbal control moment gyro systems," *J. Guidance, Control, Dyn.*, vol. 27, no. 2, pp. 271–282, 2004.

[9] B. Wie, "Singularity escape/avoidance steering logic for control moment gyro systems," *J. Guidance, Control, Dyn.*, vol. 28, no. 5, pp. 948–956, 2005.
[10] A. Berry, D. Lemus, R. Babuska, and H. Vallery, "Directional singularity-robust torque control for gyroscopic actuators," *IEEE/ASME Trans. Mechatronics*, vol. 21, no. 6, pp. 2755–2763, Dec. 2016.
[11] J. W. van. Wingerden *et al.*, "Two-degree-of-freedom active vibration control of a prototyped "Smart" rotor," *IEEE Trans. Control Syst. Technol.*, vol. 19, no. 2, pp. 284–296, Mar. 2011.
[12] I. Jikuya, K. Fujii, and K. Yamada, "Attitude maneuver of spacecraft with a variable-speed double gimbal control moment gyro," *Adv. Space Res.*, vol. 58, no. 7, pp. 1303–1317, 2016.
[13] K. Y. Lum, V. T. Coppola, and D. S. Bernstein, "Adaptive autocentering control for an active magnetic bearing supporting a rotor with unknown mass imbalance," *IEEE Trans. Control Syst. Technol.*, vol. 4, no. 5, pp. 587–597, Sep. 1996.
[14] H. Abdellatif and B. Heimann, "New experimental results on the compensation of static friction in passive joints of robotic manipulators," *IEEE Trans. Control Syst. Technol.*, vol. 18. no. 5, pp. 1005–1010, Sep. 2010.
[15] M. Ruderman and M. Iwasaki, "Sensorless torsion control of elastic-joint robots with hysteresis and friction," *IEEE Trans. Ind. Electron.*, vol. 63, no. 3, pp. 1889–1899, Mar. 2016.
[16] P. Herman, "Velocity controller with friction compensation%," *IET Control Theory Appl.*, vol. 1, no. 1, pp. 238–243, Jan. 2007.
[17] A. A. Prasov and H. K. Khalil, "A nonlinear high-gain observer for systems with measurement noise in a feedback control framework," *IEEE Trans. Autom. Control*, vol. 58, no. 3, pp. 569–580, Mar. 2013.
[18] S. B. Chaudhury, M. Sengupta, and K. Mukherjee, "Experimental study of induction motor misalignment and its online detection through data fusion," *IET Electr. Power Appl.*, vol. 7, no. 1, pp. 58–67, Jan. 2012.
[19] V. J. Lappas, W. H. Steyn, and C. I. Underwood, "Practical results on the development of a control moment gyro based on attitude control system for agile small satellites," in *Proc. AIAA/USU Small Satellite Conf.*, 2002, pp. 1–9.
[20] H. Shaker, H. Zareipour, and D. Wood, "A data-driven approach for estimating the power generation of invisible solar sites%," *IEEE Trans. Smart Grid*, vol. 7, no. 5, pp. 2466–2476, Sep. 2016.
[21] B. P. Rasmussen, A. G. Alleyne, and A. B. Musser, "Model-driven system identification of transcritical vapor compression systems," *IEEE Trans. Control Syst. Technol.*, vol. 13, no. 3, pp. 444–451, May 2005.
[22] S. A. Vaghefi, M. A. Jafai, J. Zhu, J. Brouwer, and Y. Lu, "A hybrid physics-based and data driven approach to optimal control of building cooling/heating systems," *IEEE Trans. Autom. Sci. Eng.*, vol. 13, no. 2, pp. 600–610, Apr. 2016.
[23] J. Davila, L. Fridman, and A. Levant, "Second-order sliding-mode observer for mechanical systems," *IEEE Trans. Autom. Control*, vol. 50, no. 11, pp. 1785–1789, Nov. 2005.

Sangdeok Lee (GS'17) received the B.S. and M.S. degrees in electronics engineering from Cheonbuk National University Daejeon, South Korea, in 1998 and 2003, respectively. He is currently working toward the Ph.D. degree in the Department of Mechatronics Engineering, Chungnam National University. His Ph.D. dissertation is about control moment gyroscopic actuators and its applications.

He joined LG Precision and Samsung Heavy Industries from 1998 to 2000 and from 2003 to 2014, respectively. His research interests include mechatronic system identification and control.

Seul Jung (GS'94–M'97) received the B.S. degree in electrical and computer engineering from Wayne State University, Detroit, MI, USA, in 1988, and the M.S. and Ph.D. degrees in electrical and computer engineering from the University of California, Davis, CA, USA, in 1991 and 1996, respectively.

In 1997, he joined the Department of Mechatronics Engineering, Chungnam National University, Daejeon, South Korea, where he is currently a Professor. His research interests include intelligent Mechatronics systems, intelligent robotic systems, mobile manipulators for service applications, silver ICT applications, gyroscopic motion applications, and robot education.

Dr. Jung is a member of ACA, ICROS, KROS, KIIS, KIEE, IEMEK, and IEEK.